Many-body *ab initio* study of antiferromagnetic {Cr_7M} molecular rings

A. Chiesa,[1] S. Carretta,[1] P. Santini,[1] G. Amoretti,[1] and E. Pavarini[2,3]
[1]*Dipartimento di Fisica e Scienze della Terra, University of Parma, 43124 Parma, Italy*
[2]*Institute for Advanced Simulation, Forschungszentrum Jülich, 52425 Jülich, Germany*
[3]*JARA High-Performance Computing, RWTH Aachen University, 52062 Aachen, Germany*
(Received 29 July 2016; published 20 December 2016)

Antiferromagnetic molecular rings are widely studied both for fundamental quantum-mechanical issues and for technological applications, particularly in the field of quantum information processing. Here we present a detailed first-principles study of two families—*purple* and *green*—of {Cr_7M} antiferromagnetic rings, where M is a divalent transition metal ion ($M = Ni^{2+}$, Mn^{2+}, and Zn^{2+}). We employ a recently developed flexible and efficient scheme to build *ab initio* system-specific Hubbard models. From such many-body models we systematically derive the low-energy effective spin Hamiltonian for the rings. Our approach allows us to calculate isotropic as well as anisotropic terms of the spin Hamiltonian, without any *a priori* assumption on its form. For each compound we calculate magnetic exchange couplings, zero-field splitting tensors, and gyromagnetic tensors, finding good agreement with experimental results.

DOI: 10.1103/PhysRevB.94.224422

I. INTRODUCTION

Molecular nanomagnets (MNMs) are clusters containing a finite number of paramagnetic ions, whose spins are strongly coupled by Heisenberg isotropic exchange interactions [1–3]. These finite-size systems provide a prototypical platform to understand the origin of peculiar quantum phenomena—such as coherence or tunneling—by means of a detailed and often precise spin Hamiltonian description [4,5]. Furthermore, the ability of tailoring magnetic interactions almost at will (thanks to coordination chemistry) makes these molecules attractive for potential technological applications [6–12]. In particular, compounds containing a ring of antiferromagnetically coupled transition metal ions have been heavily studied both to investigate fundamental issues [13–25] and as optimal units for the implementation of quantum information processing [8,26,27], as well as for low-temperature magnetic refrigeration [28].

Here we focus on a class of heterometallic rings in which one divalent metal ($M = Ni^{2+}$, Mn^{2+}, and Zn^{2+}) is included in an array of seven trivalent ions (Cr^{3+}). The possibility, ensured by coordination chemistry, to produce over 4000 metal octagons [29] gives a remarkable opportunity to investigate ideas in molecular magnetism. In particular, we study two representative families of {Cr_7M} compounds: the first one consists of rings which are *green* in solution and in the solid state [30], as opposed to another family of *purple* {Cr_7M} molecules [31]. The main structural difference between green and purple derivatives is the replacement of the fluoride with alkoxide within the coordination sphere of the majority of Cr^{3+} ions in the latter. This high degree of chemical control, as well as the possibility of linking Cr-based rings to form supramolecular dimers [32–34] or even more complex structures [35] and to graft them onto surfaces without altering their magnetic properties [36], has increased over the years the interest of the scientific community towards these systems. Both green and purple compounds have been extensively studied and characterized with several experimental techniques (see, e.g., Refs. [37,38]). The main technological interest of {Cr_7M} rings concerns their use as potential qubits [8,32,34], thanks to their chemical tunability and to the presence of low-lying transitions characterized by remarkably long coherence times [27,39]. At a more fundamental level, antiferromagnetic (AFM) rings are prototypical examples of correlated, finite-size quantum systems. In this respect, a detailed knowledge of the magnetic couplings is essential to correctly describe the different forms of entanglement that can arise between individual spins. Indeed, it was recently shown that the spatial modulation of pairwise entanglement can be fine-tuned by chemical substitutions [40].

Relating intramolecular magnetic interactions to the structure of a whole class of compounds would allow one both to design new systems suitable for building efficient quantum devices and to investigate fundamental quantum-mechanical issues. First-principles approaches offer the ideal tool to pursue this goal, which is typically difficult to achieve by experimental means alone. Density-functional-theory (DFT)-based methods have indeed been used for long to calculate magnetic couplings in molecular complexes [41–50]. These works rely on approximations to the universal functional, the most common of which are the local-density approximation (LDA), the generalized gradient approximation (GGA), the LDA + U approach, and, more recently, hybrid functionals. These approximations fail qualitatively, however, for strongly correlated systems. Classical examples of this failure are paramagnetic Mott insulators. For these systems LDA/GGA-type functionals yield, e.g., metallic solutions, while LDA/GGA + U open a gap, but only at the price of introducing an artifact, i.e., long-range order. For strongly correlated molecules, such as those made of ions with partially filled d or f shells, it is thus crucial to calculate the microscopic magnetic interactions accounting on the same footing for chemistry, structure, and electron-electron Coulomb interaction effects. Recently, we have shown that this can be achieved via a novel approach [51], which allows us to deduce the spin Hamiltonian starting from material-specific Hubbard models constructed *ab initio*. In the rest of the paper we call this method for simplicity DFT + MB, where MB stands for many-body. We have already used the DFT + MB technique to successfully study the magnetic interactions of prototypical compounds, finding a remarkable agreement with

experiments [51]. Other recent attempts of explicitly including many-body effects going beyond simple functionals can be found, e.g., in Refs. [52,53]. In the present work we use the DFT + MB approach to study purple and green rings and to relate the size and hierarchy of the magnetic couplings with the molecular structure. Some of these rings have been previously investigated by means of DFT calculations within a broken-symmetry calculation scheme [49]. The latter is based on performing *ab initio* total-energy calculations for different spin configurations and fitting the results to specific forms of the low-energy spin Hamiltonian [42,46,47,49]. This approach is simple to use and hence quite popular, but it has two serious drawbacks. First, it requires one to know *a priori* the form of the low-energy spin Hamiltonian, and it works best for systems well described by simple isotropic spin models; as a matter of fact, since the technique is based on fitting total-energy results, its reliability progressively declines with increasing the model complexity and thus the number of free parameters to be determined. Second, as we have mentioned above, at a more fundamental level, the simplest DFT functionals (LDA, GGA, and their simple extensions) do not properly describe strong-correlation effects in open d shells, and hybrid functionals or the LDA + U method include them only at the static mean-field level [48]. Conversely, our approach [51], by deriving spin Hamiltonians from *ab initio* system-specific Hubbard models, solves both these problems at the same time: It allows us to construct systematically spin models of arbitrary complexity and to properly account for many-body effects at the desired level. Furthermore, our method yields the full pattern of exchange and zero-field splitting interactions along the rings. The hierarchy of these interactions is found to be intimately connected with the chemical structure of the molecules. At the experimental level, this kind of information cannot be easily accessed, since available data usually allow one to determine only a minimal set of parameters describing the main interactions. To compare our results with available experimental data, we use the calculated parameters to determine physical observables and mean values, which turn out to be in good agreement with those inferred from experiments.

The paper is organized as follows. In Sec. II we describe in detail the DFT + MB method, which we employed to build spin Hamiltonians. In Sec. III we present our results for the family of purple $\{Cr_7M\}$ compounds and relate them with the corresponding analysis of the green rings. In Sec. IV we calculate physical observables and compare them with experimental findings. In Sec. V we present spin-density results. Finally, in Sec. VI we draw our conclusions.

II. MODEL-BUILDING PROCEDURE: THE DFT + MB APPROACH

A. System-specific Hubbard models

In order to construct material-specific many-body models, we follow the approach which we have introduced in Ref. [51]. We initially perform for all systems DFT calculations in the LDA approximation. Since the molecules studied in the present work have a large number of atoms, LDA calculations can be rather time-consuming. To perform them we employ the NWCHEM code [54], which is optimized to exploit the power of modern massively parallel supercomputers, and a triple-ζ valence basis set of Gaussians [55]. Next we identify and select the transition metal d-like states around the Fermi level. By using the Foster-Boys localization procedure [57] we then build a set of localized orbitals centered on the transition metal ions, which span such low-energy states. From this set of orbitals we calculate the crystal-field Foster-Boys states by diagonalizing the on-site part of the one-electron Hamiltonian (nonrelativistic calculation). We thus obtain system-specific Hubbard models:

$$\begin{aligned} H =& -\sum_{ii'}\sum_{\sigma}\sum_{mm'} t^{i,i'}_{m,m'} c^{\dagger}_{im\sigma} c_{i'm'\sigma} \\ &+ \frac{1}{2}\sum_{ii'}\sum_{\sigma\sigma'}\sum_{mm'}\sum_{pp'} U^{i,i'}_{mpm'p'} c^{\dagger}_{im\sigma} c^{\dagger}_{i'p\sigma'} c_{ip'\sigma'} c_{i'm'\sigma} \\ &+ \sum_{i}\lambda_i \sum_{mm'\sigma\sigma'} \xi^{i}_{m\sigma,m'\sigma'} c^{\dagger}_{im\sigma} c_{im'\sigma'} - H_{\mathrm{DC}} \\ =& H_T + H_U + H_{\mathrm{SO}} - H_{\mathrm{DC}}. \end{aligned} \tag{1}$$

Here $c^{\dagger}_{im\sigma}$ ($c_{im\sigma}$) creates (annihilates) a $3d$ electron with spin σ in the crystal-field Boys orbital m at site i; sites $i = 1$ to $i = 7$ are occupied by Cr^{3+} ions, while site $i = 8$ is occupied by the divalent metal ion M^{2+}, where M = Zn, Mn, and Ni. The Hamiltonian is the sum of the kinetic-energy term H_T, the Coulomb term H_U, the spin-orbit term H_{SO}, and the double-counting correction $-H_{\mathrm{DC}}$.

Let us now analyze term by term the Hamiltonian (1), starting from H_T. The parameters $t^{i,i'}_{m,m'}$ appearing in H_T yield the hopping integrals ($i \neq i'$) or the crystal-field matrix ($i = i'$). The latter is diagonal in the crystal-field basis; we denote the energy of the crystal-field orbitals with $\varepsilon_m = t^{i,i}_{m,m}$ and order them such that $\varepsilon_m \leqslant \varepsilon_{m+1}$. Figure 1 shows the crystal-field orbitals for the Mn^{2+} ion in a purple Cr_7Mn wheel. They exhibit the typical form of d orbitals in a quasioctahedral environment: a lower energy t_{2g}-like quasitriplet [Figs. 1(a)–1(c)] and a 1- to 2-eV higher-energy e_g-like quasidoublet [Figs. 1(d) and 1(e)].

The terms $U^{i,i'}_{mpm'p'}$ entering in H_U are the screened Coulomb integrals. For simplicity here we use the rotationally invariant Kanamori form of the Coulomb vertex; the neglected terms, Coulomb orbital anisotropy and terms with more than two orbital indices, yield small corrections to the spectrum of the systems studied in the present paper. In this approximation all Coulomb parameters can be expressed as a function of the averaged screened Coulomb couplings $U^{i,i} = U$ and $J^{i,i} = J$, which, in turn, depend only on the Slater integrals F_0, F_2, and F_4 [58]. The essential terms in H_U are thus the direct [$U^{i,i}_{mm'mm'} = U_{m,m'} = U - 2J(1 - \delta_{m,m'})$] and the exchange ($U^{i,i}_{mm'm'm} = J$) interaction, the pair-hopping term ($U^{i,i}_{mmm'm'} = J$), and the spin-flip term ($U^{i,i}_{mm'm'm} = J$). The last two interactions are crucial to determine the correct structure of the spin multiplets. We calculate U and J via the constrained local-density approximation (cLDA) [59] approach in the Foster-Boys basis, keeping the basis frozen in the self-consistency loop.

The term H_{DC} is the double-counting correction, which removes the mean-field part of the local Coulomb interaction,

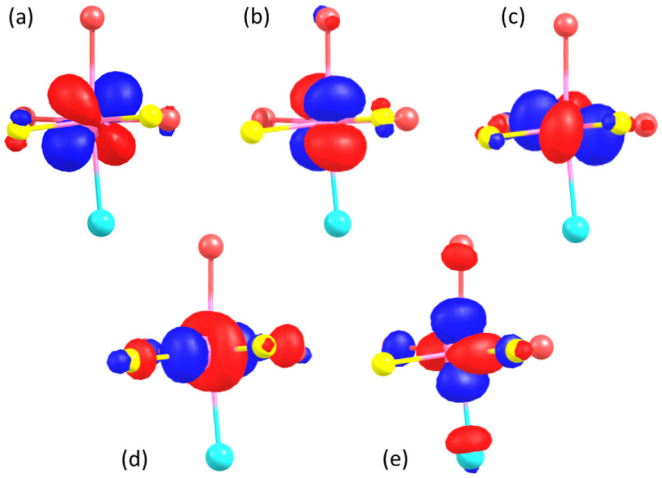

FIG. 1. Crystal field d orbitals, obtained by diagonalization of the crystal-field matrix $t^{i,i}_{m,m'}$ for i = Mn (purple ring), in order (a) to (e) of increasing energy. Red (blue) orbital lobes are positive (negative). The quasioctahedral environment is reflected in the crystal-field states: a lower-energy t_{2g}-like quasitriplet (a)–(c) and a 1- to 2-eV higher-energy e_g-like quasidoublet (d)–(e). In the plot only the Mn quasioctahedral cage is shown (Mn is purple, O is red, F is yellow, and N is cyan).

already included in the LDA. Here we adopt the fully localized limit [58], which is more appropriate for molecular systems. Hence $H_{\rm DC} = \frac{1}{2}\sum_i U^{i,i} n^i_d(n^i_d - 1) - \frac{1}{4}\sum_i J^{i,i} n^i_d(\frac{1}{2}n^i_d - 1)$, where n^i_d is the number of d electrons at site i. In the case of homonuclear systems such correction amounts to a shift of the d levels, $\varepsilon^i_m \to \varepsilon^i_m + \Delta\varepsilon^i_m$, where $\Delta\varepsilon^i_m = -U^{i,i}(n^i_d - \frac{1}{2}) + J^{i,i}(\frac{1}{2}n^i_d - \frac{1}{2})$, which is the same for all sites and orbitals, and can be incorporated in the chemical potential; for heteronuclear compounds, instead, the shift $\Delta\varepsilon^i_m$ is site dependent and $H_{\rm DC}$ has to be taken into account explicitly.

Finally, λ_i, entering in the term $H_{\rm SO}$, is the strength of the spin-orbit interaction, here the same for all the $3d$ electrons within the same ion. The elements $\xi^i_{m\sigma,m'\sigma'} = \langle m\sigma|\mathbf{s}^i \cdot \mathbf{l}^i|m'\sigma'\rangle$ are matrix elements of the spin-orbit matrix in the Forster-Boys basis. The coupling λ_i can be extracted by comparing the single-electron crystal-field splittings with and without spin-orbit interaction, as we have shown in Ref. [51]. In this work, since relativistic self-consistent calculations are very time-consuming and the spin-orbit coupling is basically a property of the single ion (in its local environment, which for all systems considered here is approximately octahedral), for λ_i we use either values previously determined by us via our method for similar systems [51] or tabulated values for the same ions in a similar environment [60]. We had indeed proved in Ref. [51] that the latter is a very good approximation for this kind of systems.

The representative crystal-field parameters and the essential Coulomb integrals for the system considered in this work, obtained with the method described above, are given in Table I.

B. Low-energy spin models

In this section we explain how, starting from the Hubbard model (1), we obtain for each molecule the corresponding low-energy spin model. Let us start, however, from the conclusion and then explain the derivation of all terms one by one. For all systems analyzed in this work, we find that the essential magnetic interactions are described by the following spin Hamiltonian:

$$\begin{aligned} H_{\rm S} &= \frac{1}{2}\sum_{\langle i\neq i'\rangle}\Gamma^{i,i'}\mathbf{S}_i\cdot\mathbf{S}_{i'} + \sum_i[\mathbf{S}_i\cdot\underline{\mathbf{D}}^i\cdot\mathbf{S}_i + \mu_B\mathbf{B}\cdot\underline{\mathbf{g}}^i\cdot\mathbf{S}_i] \\ &\quad + \sum_{i\neq i'}\mathbf{S}_i\cdot\underline{\mathcal{D}}^{i,i'}\cdot\mathbf{S}_{i'} \\ &= H_{\rm EX} + \sum_i\left[H^i_{\rm ZFS} + H^i_{\rm Z}\right] + H_{\rm DIP}, \end{aligned} \tag{2}$$

where $\Gamma^{i,i'}$ are the isotropic exchange couplings, the sum over $\langle i \neq i'\rangle$ is restricted to first-nearest-neighbor atoms, $\underline{\mathbf{D}}^i$ is the local zero-field splitting (ZFS) tensor, and the third term describes the Zeeman interaction with an external magnetic field $\mathbf{B}$. The last term describes magnetic dipole-dipole interactions with couplings $\underline{\mathcal{D}}^{i,i'}$ calculated in the point-dipole approximation [1], using the $\underline{\mathbf{g}}^i$ tensors derived *ab initio* (see below). The magnetic exchange coupling $\Gamma^{i,i'} = \Gamma^{i,i'}_{\rm CE} + \Gamma^{i,i'}_{\rm SE}$ is the sum of a ferromagnetic (FM) screened Coulomb exchange term, $\Gamma^{i,i'}_{\rm CE}$, which we obtain via cLDA calculations, and the superexchange contribution $\Gamma^{i,i'}_{\rm SE}$, which we obtain via many-body perturbation theory. The latter can in principle be either FM or AFM; for all systems considered in this work it turns out to be AFM. Finally, for all the examined molecules, we find that other terms, such as the anisotropic or antisymmetric exchange interactions and the higher-order zero-field splitting parameters, are negligible.

To derive Hamiltonian (2) from Hamiltonian (1) we proceed as follows. First, by using a canonical transformation [62], we eliminate charge fluctuations and derive from the Hubbard model the corresponding low-energy spin model. Since for the systems analyzed in this work $|t^{i,i'}_{m,m'}| \ll U^{i,i}$ (see Table I) the expansion can be basically truncated at the second-order perturbation theory level. This expansion systematically yields the couplings $\Gamma^{i,i'}_{\rm SE}$, which in turn, added to the ferromagnetic

TABLE I. Top: Crystal-field levels (in eV) for one representative Cr ion and for Mn and Ni ions, in the cases of both purple and green rings. The lowest-energy crystal-field level is taken as the zero. Bottom: Screened Coulomb integrals $U^{i,i}$ and $J^{i,i}$ obtained via cLDA (in eV) and spin-orbit coupling λ_i (in meV) [61].

	Purple			Green		
	Cr	Mn	Ni	Cr	Mn	Ni
$\|n\rangle$			ε_n			
$\|1\rangle$	0.000	0.000	0.000	0.000	0.000	0.000
$\|2\rangle$	0.081	0.081	0.088	0.010	0.051	0.077
$\|3\rangle$	0.117	0.219	0.250	0.133	0.249	0.206
$\|4\rangle$	2.098	1.387	1.204	2.031	2.275	1.376
$\|5\rangle$	2.222	1.476	1.284	2.141	2.347	1.519
			Coulomb integrals			
$U^{i,i}$	6.00	6.49	6.30	5.98	6.32	6.28
$J^{i,i}$	0.30	0.35	0.21	0.26	0.34	0.23
λ_i	16.5	20.7	33.5	16.5	20.7	33.5

Coulomb exchange term, gives $\Gamma^{i,i'}$ and thus the exchange term $H_{\rm EX}$ in Hamiltonian (2).

Next, we calculate the zero-field splitting tensor for each atom, i.e., the terms $H^i_{\rm ZFS}$. To this end, we first diagonalize the on-site part of Hamiltonian (1), without, however, the spin-orbit term; i.e., we diagonalize the Coulomb and crystal-field terms. This yields the ionic multiplets in the molecular environment, of course in the absence of spin-orbit interaction. Since for the systems analyzed here the ground-state and excited-state multiplets are well separated in energy and the hopping integrals are small with respect to the Coulomb interaction, we can assume that each ion is, in first approximation, in the n^i_d-electron ground-state multiplet, with a well-defined spin S_i. More specifically, we find a stable triplet ground state for Ni^{2+}, a sextet for Mn^{2+}, and a quartet for all Cr^{3+} ions, with spins $S = 1$, $S = 5/2$, and $S = 3/2$, respectively. Up to now we neglected the spin-orbit interaction. Since, for the ions considered here, the latter is small with respect to the Coulomb energy splittings or the crystal-field splitting, for all cases considered here, it is sufficient to treat its effects as a perturbation up to second order. If we denote with $|\Psi^i_l(n)\rangle$ the n-electron eigenstate with energy $E^i_l(n)$, and $E^i_0(n^i_d)$ is the energy of the ground-state multiplet, we thus have

$$\langle\Psi^i_k(n^i_d)|H^i_{\rm ZFS}|\Psi^i_{k'}(n^i_d)\rangle = \sum_l \frac{\langle\Psi^i_k(n^i_d)|H^i_{\rm SO}|\Psi^i_l(n^i_d)\rangle\langle\Psi^i_l(n^i_d)|H^i_{\rm SO}|\Psi^i_{k'}(n^i_d)\rangle}{E^i_0(n^i_d) - E^i_l(n^i_d)}.$$

Here l labels the states of the excited n^i_d-electron multiplets; k and k' label instead the states within the ground multiplet. Recasting the zero-field splitting tensor into the basis of the eigenvectors of $S_{z,i}$ and decomposing by scalar product into Stevens operators $O^q_k(\mathbf{S}_i)$, we find $H^i_{\rm ZFS} = \sum_q b^q_2(i) O^q_2(\mathbf{S}_i)$ and the corresponding zero-field tensor $\underline{\mathbf{D}}^i$. Finally, we can express $\underline{\mathbf{D}}^i$ in the (local) reference frame which diagonalizes it; in such a reference frame the zero-field splitting interaction can be expressed as the sum of an axial term, d^i, and a rhombic term, e^i, i.e.; it takes the form

$$H^i_{\rm ZFS} = d^i\left[S^2_{z,i} - \tfrac{1}{3}S_i(S_i+1)\right] + e^i\left[S^2_{x,i} - S^2_{y,i}\right].$$

By diagonalizing the tensor $\underline{\mathbf{D}}^i$ we thus also determine the principal anisotropy axes on each magnetic ion. Notice that, if $|e_i/d_i| \ll 1$, the case of the systems considered here, $d^i < 0$ implies that z is an easy axis.

At last we calculate the gyromagnetic tensor $\underline{\mathbf{g}}^i$ and hence the Zeeman term H^i_Z in the spin Hamiltonian. In the ground-state multiplet, in the absence of spin-orbit interaction, the gyromagnetic tensor is diagonal, i.e., $\underline{\mathbf{g}}^i = 2I$, where I is the identity matrix. The anisotropic contributions come from the spin-orbit effects; to calculate them we thus first correct the ground spin multiplet states to first order in $H_{\rm SO}$, obtaining a new wave function, $\tilde\Psi^i_k(n^i_d) \sim \Psi^i_k(n^i_d) + \Delta\Psi^i_k(n^i_d)$, where

$$\Delta\Psi^i_k(n^i_d) \sim \sum_l \frac{|\Psi^i_l(n^i_d)\rangle\langle\Psi^i_l(n^i_d)|H^i_{\rm SO}|\Psi^i_k(n^i_d)\rangle}{E^i_0(n^i_d) - E^i_l(n^i_d)}. \quad (3)$$

The anisotropic contribution to the gyromagnetic tensor $\Delta g_{\alpha\alpha'}$ is then given by

$$\langle\tilde\Psi^i_k(n^i_d)|L_{\alpha,i}|\tilde\Psi^i_{k'}(n^i_d)\rangle = \sum_{\alpha'}\Delta g_{\alpha\alpha'}\langle\Psi^i_k(n^i_d)|S_{\alpha',i}|\Psi^i_{k'}(n^i_d)\rangle.$$

In the actual calculations it is sufficient to retain only first-order correction in the spin-orbit coupling, since the second-order terms turn out to be negligible.

III. RESULTS FOR {Cr_7M} RINGS

In this section we describe the actual results for the two families of molecules studied in the present work.

A. Purple rings

The superexchange and Coulomb-exchange parameters obtained for each couple of neighboring ions in purple rings are listed in Table II. It is interesting to compare the results with the molecular structure, shown in Fig. 2. If we consider all possible couples of nearest-neighboring Cr, we find essentially two well distinguishable values of the exchange couplings, associated with two very different types of superexchange paths. As it can be seen in Fig. 2(a), the first type involves two carboxylate bridges and an oxygen bridge (oxygen ions are red in the figure); this type of superexchange path is relevant for all the couples Cr_i-Cr_{i+1} with $2 \leqslant i \leqslant 6$. The second kind of path involves, instead, two carboxylate and a fluorine (fluorine ions are yellow in Fig. 2) bridge, and it is relevant only for the Cr_1-Cr_2 bond. The exchange coupling associated with the fluorine-type path is substantially smaller than the exchange couplings stemming from paths without fluorine. Indeed, we find that both the overlap between localized neighboring orbitals and the hopping integrals are larger for the bond involving an O with respect to the case in which the oxygen is replaced by fluorine. An additional path is provided by the Cr-O-C-C-O-Cr bridge, as can be seen in Fig. 2(b); this is, however, longer than the others and gives correspondingly only a small contribution to the exchange couplings. The effect of the fluorine substitution in decreasing the exchange coupling was previously suggested in Ref. [63] based on broken-

TABLE II. Calculated superexchange ($\Gamma^{i,i'}_{\rm SE}$) and Coulomb-exchange ($\Gamma^{i,i'}_{\rm CE}$) couplings, for each pair of nearest neighbors in the examined families of rings (in meV). The fourth and last columns report the total $\Gamma^{i,i'} = \Gamma^{i,i'}_{\rm SE} + \Gamma^{i,i'}_{\rm CE}$.

	Purple			Green		
Bond	$\Gamma^{i,i'}_{\rm SE}$	$\Gamma^{i,i'}_{\rm CE}$	$\Gamma^{i,i'}$	$\Gamma^{i,i'}_{\rm SE}$	$\Gamma^{i,i'}_{\rm CE}$	$\Gamma^{i,i'}$
Cr_1-Cr_2	1.89	−0.41	1.48	2.07	−0.38	1.69
Cr_2-Cr_3	2.93	−0.51	2.42	1.89	−0.33	1.56
Cr_3-Cr_4	2.86	−0.43	2.43	2.03	−0.33	1.70
Cr_4-Cr_5	2.94	−0.49	2.45	1.88	−0.32	1.56
Cr_5-Cr_6	3.04	−0.60	2.44	2.09	−0.31	1.78
Cr_6-Cr_7	3.14	−0.49	2.65	1.90	−0.29	1.61
Cr_7-Mn	1.80	−0.35	1.45	1.92	−0.29	1.63
Mn-Cr_1	2.34	−0.52	1.82	1.66	−0.27	1.39
Cr_7-Ni	2.47	−0.36	2.11	2.22	−0.40	1.82
Ni-Cr_1	3.02	−0.50	2.52	2.03	−0.36	1.67

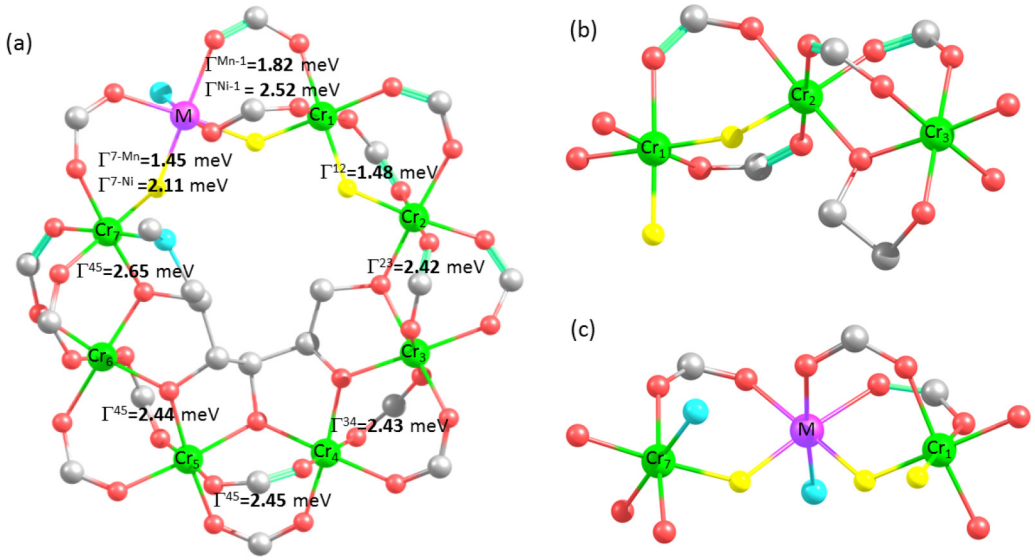

FIG. 2. (a) Molecular structure of the purple $\{Cr_7M\}$ (M = Ni and Mn) family of compounds, with calculated isotropic exchange couplings (in meV) for each pair of nearest-neighboring magnetic ions. H atoms are not shown for clarity, while C are gray, N are light blue, F are yellow, O are red, Cr are green, and M (= Ni and Mn) is purple. The value of the exchange couplings crucially depends on whether or not a fluorine replaces oxygen in the superexchange path. The different types of possible superexchange paths can be seen more clearly in the fragments shown in panel (b) for the Cr-Cr bonds and in panel (c) for the Cr_7-M and M-Cr_1 bonds.

symmetry calculations; our results confirm this hypothesis, evidencing the microscopic mechanism behind this conclusion and quantifying the difference between the bonds. A similar analysis on the Cr-M bonds evidences instead the important role played by the carboxylate groups in the superexchange interactions. For both Cr_7Mn and Cr_7Ni, we find $\Gamma^{7,8} < \Gamma^{8,1}$, where 8 is the M site. These results can be understood by examining Fig. 2(c): an additional carboxylate superexchange path is present in the M-Cr_1 bond which is absent in the Cr_7-M bond.

We now examine the anisotropic terms of the spin Hamiltonian. Table III reports the local ZFS parameters d^i and $|e^i|$ along with the rhombicity factor $|e^i/d^i|$ for purple rings.

TABLE III. Calculated local zero-field splitting parameters (in μeV) for the purple and green $\{Cr_7M\}$ rings. For each magnetic ion, d^i and $|e^i|$ are the axial term and the rhombic term in the reference frame given by the local principal axes of the $\underline{\mathbf{D}}^i$ tensor. We find easy-axis anisotropy for all ions except for Mn^{2+} and Zn^{2+}; the latter is diamagnetic. The fourth and last columns report the rhombicity factor $|e^i/d^i|$.

	Purple			Green		
	d^i	$\lvert e^i\rvert$	$\lvert e^i/d^i\rvert$	d^i	$\lvert e^i\rvert$	$\lvert e^i/d^i\rvert$
Cr_1	−31	6	0.19	−65	10	0.15
Cr_2	−40	7	0.16	−46	6	0.13
Cr_3	−29	8	0.27	−37	5	0.14
Cr_4	−74	17	0.23	−78	11	0.14
Cr_5	−45	8	0.18	−68	9	0.13
Cr_6	−84	25	0.30	−55	8	0.15
Cr_7	−49	9	0.18	−63	10	0.16
Mn	−15	1	0.09	6	0	0.00
Ni	−804	162	0.20	−480	29	0.06

Figure 3 shows the local z axes for purple Cr_7Mn; they basically follow the direction of the lobes of the highest-energy crystal-field orbitals. These are found to be almost perpendicular to the plane of the ring for all the ions, except for the Cr next to the M ion (on the right in Fig. 3), for which the tilt angle between the local z axis and the global Z axis (perpendicular to the plane of the ring) is about 40°. Conversely, the local x and y axes are rotated from ion to ion, following the directions of the ligands in the crystal cage.

Finally, we discuss the gyromagnetic tensor. First of all, we find that in all systems considered here basically the same system of local axes diagonalize both the zero-field splitting

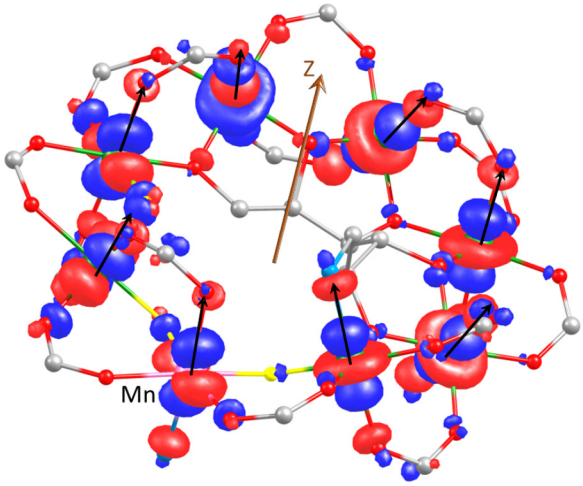

FIG. 3. Highest-energy crystal-field orbital for each magnetic ion and direction of the local z axes for purple Cr_7Mn. CH_3 groups are not shown for clarity. The brown arrow indicates the global Z axis (perpendicular to the plane of the ring). The Mn ion is located in the bottom left part of the figure.

TABLE IV. Principal components of the $\underline{\mathbf{g}}$ tensor for Ni^{2+} ions in purple and green Cr_7Ni rings. Available experimental values (fitted from electron paramagnetic resonance data) [37] are shown in brackets. The tensor is given in the local coordinate system which diagonalizes simultaneously $\underline{\mathbf{g}}^i$ and the zero-field tensor $\underline{\mathbf{D}}^i$.

	g_{xx}		g_{yy}		g_{zz}	
Purple	2.08	(2.18)	2.16	(2.18)	2.28	(2.25)
Green	2.07	(–)	2.08	(–)	2.15	(–)

tensor and the gyromagnetic tensor. Second, we find that the anisotropic correction to the $\underline{\mathbf{g}}^i$ tensor is very small for Cr and Mn ions in all the examined molecules, both green and purple types. For instance, in the case of Cr^{3+} ions, we get for all systems $1.98 < g_{\alpha\alpha} < 2$ (referred to the local principal axes). We find the largest effects of anisotropy on the gyromagnetic tensors in the case of Ni^{2+} ions, whose values are given in Table IV (first line).

B. *Green* rings

A similar analysis can be done for the green variants of $\{Cr_7M\}$ antiferromagnetic rings. Figure 4 shows the distribution of the exchange constants. We find that they are more uniform along the ring than in the case of the purple family of compounds. This can be directly related to the structure. Indeed, in the green variant the superexchange paths *always* involve a single fluorine bridge and two carboxylates, as opposed to the more complex structure of bridges found in the purple complexes. The value of all fluorine-mediated exchange couplings are similar in the purple and the green variant of the ring [51]. However, we note that the calculated exchange couplings show an ABAB pattern which reflects the alternated orientation of the carboxylate groups, above or below the plane of the molecule (see Fig. 4). This is consistent with a previous analysis of inelastic neutron scattering data on the parent Cr_8 green compound [17], where it was shown that a model with an alternated pattern of exchange constants produces the same low-energy spectrum as that with uniform exchange constants.

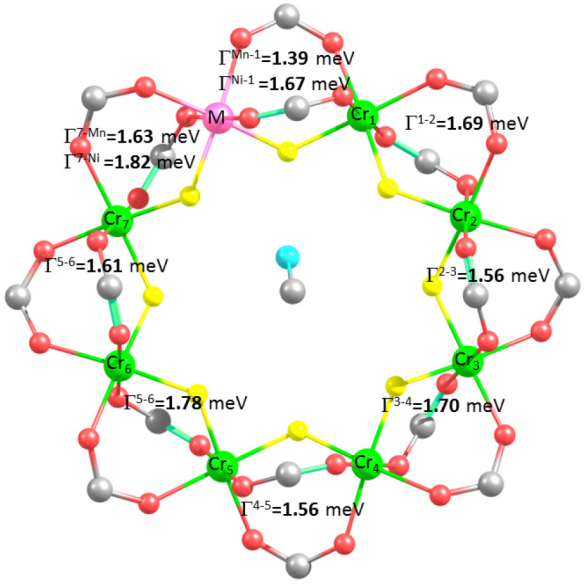

FIG. 4. Molecular structure and calculated exchange integrals of the green rings.

The zero-field splitting microscopic parameters for the green rings are listed in Table III. Similarly to what was observed for the purple derivatives, the local z axes turn out to be almost perpendicular to the plane of the ring, while the local x and y axes follow the direction of the ligands in the crystal cage. As far as Cr ions are concerned, the average absolute value of their local axial anisotropy is slightly larger in the green variants than in the purple variants (-0.06 vs -0.05 meV), a trend which is also in agreement with electronic absorption spectra reported in Ref. [37]. We find the largest effects of anisotropy in the case of Ni^{2+} ions, in both families of compounds, with $|d^{\mathrm{Ni}}_{\mathrm{green}}| = 0.48$ meV $< |d^{\mathrm{Ni}}_{\mathrm{purple}}| = 0.80$ meV. The larger value of $|d^{\mathrm{Ni}}|$ calculated for the purple Cr_7Ni wheel is due to the smaller excitation energies appearing in the denominator of Eq. (3); smaller splittings originate from the smaller Coulomb exchange integrals and crystal-field gaps which we obtained in the purple case, induced by the larger elongation of the octahedral cage in purple with respect to green compounds. The rhombic distortion of the ligands surrounding the Ni ion is also more pronounced in purple rings, leading to a sizably larger calculated rhombicity (0.23 vs 0.06).

Let us finally discuss the gyromagnetic tensor. The smaller excitation energies are also responsible for the larger $\Delta\underline{\mathbf{g}}^i$ for the purple variant with respect to its green analog (see Table IV). Finally, due to the larger distortion of the ligand cage, the g_{xx} and g_{yy} components of the $\underline{\mathbf{g}}^{\mathrm{Ni}}$ tensor differ much more with respect to each other in the purple variant than in the green variant (in agreement with the larger rhombicity displayed by purple rings).

IV. COMPARISON WITH EXPERIMENTS

The spin models used to fit experimental data in Refs. [37,38] assume only two values for the exchange couplings ($\Gamma^{\mathrm{Cr,Cr}}$ and $\Gamma^{\mathrm{Cr},M}$) and two values of the ZFS axial parameters (d^{Cr}, d^M), the same for all the homonuclear sites on the rings. Therefore, to compare with experiments, we use two approaches.

In the first approach we compute the average values:

$$\Gamma^{\mathrm{Cr,Cr}} = \frac{1}{6}\sum_{i=1}^{6}\Gamma^{i,i+1}, \quad \Gamma^{\mathrm{Cr},M} = \frac{1}{2}[\Gamma^{8,1} + \Gamma^{7,8}].$$

These values are reported in Table V for both green and purple compounds, where they are also compared with the corresponding experimental estimates. It is worth noting that for all systems considered, our results are closer to experimental findings than those obtained by total-energy spin-configuration calculations based on the B3LYP functional [49] (in which uniform exchange constants are assumed from the start). Moreover, the hierarchy of interactions among different compounds is correctly reproduced (for both green and purple families, $\Gamma^{\mathrm{Cr,Mn}} < \Gamma^{\mathrm{Cr,Cr}} < \Gamma^{\mathrm{Cr,Ni}}$).

TABLE V. Comparison between calculated and (in parentheses) experimentally determined [37,38] isotropic exchange parameters for the green and purple $\{Cr_7M\}$ rings. The calculated values are averaged along the ring.

	$\Gamma^{Cr,Cr}$ (meV)		$\Gamma^{Cr,M}$ (meV)	
	Green	Purple	Green	Purple
Cr_7Zn	1.65 (1.46)	2.31 (1.72)	0 (0)	0 (0)
Cr_7Ni	1.65 (1.46)	2.31 (1.72)	1.75 (1.70)	2.32 (2.59)
Cr_7Mn	1.65 (1.46)	2.31 (1.72)	1.49 (1.37)	1.63 (1.03)

The second approach that we adopt to put our results to the experimental test consists of calculating specific exchange splittings that can be or have been actually measured. To this end, first we diagonalize the isotropic part of our spin Hamiltonian and compare the results directly with experimental inelastic neutron scattering peaks [37,38]. Results are shown in the left side of Table VI and are in good agreement (within ∼30%) with experiments.

For all the examined systems isotropic exchange is the dominant interaction. Hence, the spectrum obtained by diagonalization of the full spin Hamiltonian practically consists of spin multiplets split by the anisotropic terms of the spin Hamiltonian, i.e., the on-site zero-field tensor and the two-body magnetic dipole-dipole terms of H_S [Eq. (2)]. Hence, analyzing these splittings allows us to test the anisotropic terms of the spin Hamiltonian. The right side of Table VI reports the calculated splitting of the lowest-lying spin $\mathcal{S} > 1/2$ multiplet, compared with the levels derived from the positions of the peaks measured by inelastic neutron scattering and attributed to the investigated transitions [37,38]. In the last column of the table the sign of the effective molecular anisotropy (easy plane or easy axis) is also reported and compared with experimental findings (in parentheses). The agreement between experiments and theory is good and the sign is always correct. In particular, we find easy plane anisotropy for Cr_7Ni and easy axis for Cr_7Mn and for Cr_7Zn. It is worth pointing out that also the trend of the experimental gaps is well reproduced, with the largest gap found for Cr_7Ni and similar splittings for Cr_7Mn and Cr_7Zn (in both purple and green derivatives). Notice that the $\mathcal{S} = 3/2$ multiplet splits into two doublets (due to Kramers degeneracy). Conversely, the $\mathcal{S} = 1$ multiplet could in principle split into three singlets, but two of them are almost degenerate (for both calculated and measured spectra) and hence only the most relevant gap is reported. We stress that the subtle anisotropic interactions giving rise to these splittings are not usually extracted by broken-symmetry calculations, in which, to avoid overparametrization, the Heisenberg exchange is assumed to be the only relevant term of the Hamiltonian. Conversely, we systematically derive the full spin Hamiltonian without any assumption on its form. Finally, it is worth noting that the overlap between the ground state of our microscopic spin Hamiltonian (2) and that of the spin Hamiltonian obtained by fitting experiments [37] is very large: the squared scalar product of the two states is indeed 0.975.

V. SPIN DENSITY

In this section we present electronic spin-density calculations. Nuclear magnetic resonance [64,65] and polarized neutron diffraction [66] techniques have recently allowed a direct and quantitative measurement of the spatial distribution of the spin moments (integrated spin density) within antiferromagnetic molecular rings. These data provide fundamental signatures of the topology (open/closed) and parity effects (even/odd) in finite spin chains. Representative calculations for two $\{Cr_7M\}$ purple rings are shown in Fig. 5, but perfectly analogous results are also obtained for the corresponding green variants. The electron spin density is given by the expectation value $\langle \mathcal{S}_z(\mathbf{r}) \rangle$, where

$$\mathcal{S}_z(\mathbf{r}) \approx \frac{1}{2} \sum_{i,m} [c^\dagger_{im\uparrow} c_{im\uparrow} - c^\dagger_{im\downarrow} c_{im\downarrow}] |\phi_{im}(\mathbf{r})|^2$$

is the third component of the total spin operator. Here $\phi_{im}(\mathbf{r})$ are crystal-field orbitals which account for the spatial dependence of the spin density. The shape of the spin densities is directly related to the symmetry of the occupied crystal-field orbitals. As previously discussed, since in the molecules considered here all magnetic ions are surrounded by a slightly distorted octahedral environment, the transition metal d orbitals split into a lower-energy t_{2g}-like quasitriplet and a higher-energy e_g-like quasidoublet. In the absence of a magnetic field the spin polarization in the ground state is zero. An external magnetic field lifts the degeneracy of the

TABLE VI. Left: Splitting (in meV) between total spin ground-state $\mathcal{S}$ and first excited multiplet $\mathcal{S}'$, calculated starting from our microscopic spin Hamiltonian; in parentheses, the same splitting measured by inelastic neutron scattering [37,38]. The spins $\mathcal{S}$ and $\mathcal{S}'$ are given in the next column. Right: Calculated splitting (first column, in meV) of the lowest energy $\mathcal{S} > 1/2$ multiplet (second column), induced by anisotropic terms of the spin Hamiltonian. In the third column the sign of the axial contribution to the effective molecular anisotropy (+ = easy plane/ − = easy axis) is given. Experimental values [37,38] are in parentheses.

Compound		Exchange		ZFS		
		Gap	$\mathcal{S} \to \mathcal{S}'$	Gap	$\mathcal{S}$	Sign of the axial contrib.
Green	Cr_7Zn	0.95 (0.84)	$3/2 \to 1/2$	0.18 (0.11)	3/2	− (−)
	Cr_7Ni	1.38 (1.24)	$1/2 \to 3/2$	0.24 (0.14)	3/2	+ (+)
	Cr_7Mn	1.68 (1.52)	$1 \to 2$	0.16 (0.10)	1	− (−)
Purple	Cr_7Zn	1.20 (1.00)	$3/2 \to 1/2$	0.12 (0.09)	3/2	− (−)
	Cr_7Ni	1.81 (1.50)	$1/2 \to 3/2$	0.26 (0.14)	3/2	+ (+)
	Cr_7Mn	2.18 (1.48)	$1 \to 2$	0.12 (0.08)	1	− (−)

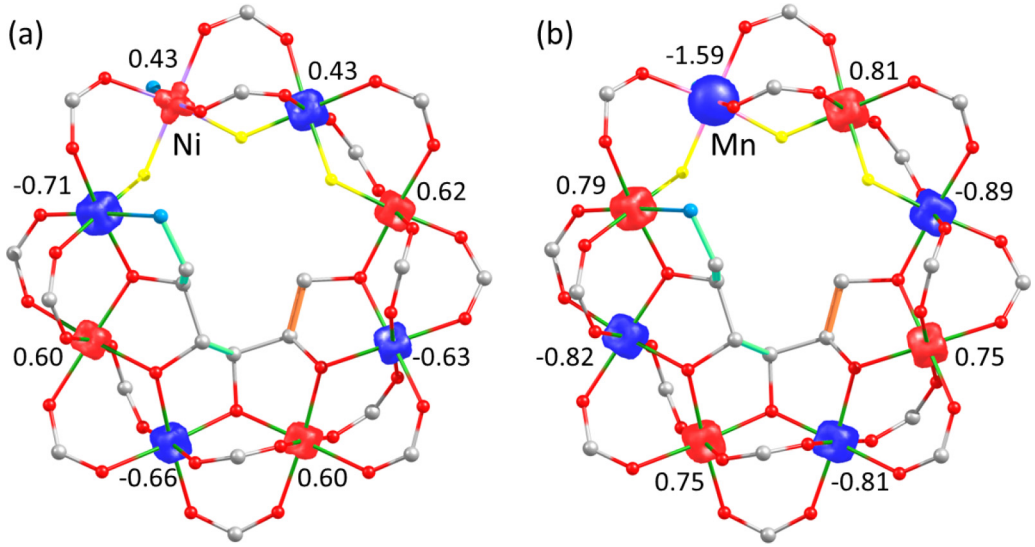

FIG. 5. Spin density on the ground state of $\{Cr_7M\}$ purple rings, $\langle \mathcal{S}_z(\mathbf{r})\rangle$, in an applied field perpendicular to the ring of 5 T. Isovalues of 0.04 electrons/a.u. have been used. Different colors correspond to the positive (red) and negative (blue) values of the spin density. CH_3 groups are not shown for clarity. (a) Cr_7Ni ring, characterized by a ground spin state, $|\mathcal{S} = 1/2, \mathcal{M} = -1/2\rangle$; (b) Cr_7Mn, which shows $|\mathcal{S} = 1, \mathcal{M} = -1\rangle$. The calculated local spin moments are reported close to each magnetic ion.

ground multiplets, yielding a spin polarization. The resulting spin density is sizable around the magnetic ions of the ring. In particular, Cr^{3+} is in the t_{2g}^3 electronic configuration; thus, in the presence of a magnetic field, the spin polarization mostly arises from t_{2g} states. This can be seen from the fact that the shape of the spatial distribution of the spin density around each atom is cubiclike, because the lobes of these orbitals extend around the diagonals of the orthorhombic axes. Instead, Mn^{2+} and Ni^{2+} have five and eight electrons in the d shell, respectively. Hence, Mn displays the typical sphere-shaped spin density of an S ion, due to the polarization of both t_{2g}-like and e_g-like states, while the star-shaped spin density of Ni originates from the polarization of e_g-like orbitals (the t_{2g} states are fully occupied). The figure shows that the spin polarization has opposite signs at Ni and Mn sites. This reflects the fact that, compared to the spin on the neighboring Cr ions, Ni has a smaller and Mn a larger magnetic moment; hence the spin of Mn tends to align antiparallel to the magnetic field; to make this more clear, in Fig. 5 we give the distribution of local spin moments along the rings. The magnetic field is applied along the global Z direction (perpendicular to the plane of the ring). The calculated spin moments for the green Cr_7Ni and Cr_7Zn are close to those derived in Refs. [64,65] from the analysis of the nuclear magnetic resonance spectra of ^{53}Cr and ^{19}F.

VI. CONCLUSIONS

Summarizing, we have presented a detailed *ab initio* many-body study of two families of antiferromagnetic $\{Cr_7M\}$ molecular rings. The study is performed by means of the recently developed DFT + MB approach [51], which is based on the construction of system-specific many-body Hubbard-like models, using a basis of localized Foster-Boys orbitals. Our method allows us to deduce the full spin Hamiltonian without any *a priori* assumption on its form and with no free parameters. By explicitly including strong correlation effects beyond the static mean-field level, we achieve a good agreement between calculated and experimental results. The spin-orbit interaction tensor is calculated by comparing the Hubbard model obtained from classic and relativistic calculations. In this work, in order to reduce the computational cost, we use spin-orbit couplings either determined by us in Ref. [51] or tabulated for the same ions in similar environments; we proved in test cases that this is indeed a very good approximation. The successful application of the DFT + MB approach to a wide class of Cr_7M molecular rings demonstrates the effectiveness of our scheme. Moreover, we obtain the full pattern of exchange and zero-field splitting terms, a kind of information which is hardly accessible even with the most advanced experimental techniques and is typically not extracted by standard broken-symmetry calculations. This allows us to relate the superexchange paths with the molecular structure, thus enabling a deeper understanding of the origin of magnetic interactions and the design of suitable devices for future quantum technologies. Indeed, the present study highlights how magnetic couplings and zero-field splittings can be tailored by chemically engineering the cage of the magnetic ions, thus controlling static and dynamic properties of molecular nanomagnets. The determination of individual exchange couplings and subtle anisotropic terms of the spin Hamiltonian is essential to provide an accurate description of molecular magnets. These terms have a key role in controlling the entanglement between composite subsystems of the molecular cluster, whose detection (by four-dimensional inelastic neutron scattering [22,67]) is at the forefront of current research.

ACKNOWLEDGMENTS

This work was financially supported by the Italian FIRB Project No. RBFR12RPD1 of the Italian MIUR "New

Challenges in Molecular Nanomagnetism: From Spin Dynamics to Quantum-Information Processing." Calculations were done on the Jülich supercomputer Jureca. E.P. acknowledges financial support from the Deutsche Forschungsgemeinschaft through Research Unit FOR1346. A.C. acknowledges "Centro Universitario Cattolico" for supporting this project.

[1] D. Gatteschi, R. Sessoli, and J. Villain, *Molecular Nanomagnets* (Oxford University Press, London, 2006).
[2] M. Mannini, F. Pineider, C. Danieli, F. Totti, L. Sorace, Ph. Sainctavit, M. A. Arrio, E. Otero, L. Joly, J. C. Cezar, A. Cornia, and R. Sessoli, Nature (London) **468**, 417 (2010).
[3] M. Mannini, F. Pineider, P. Sainctavit, C. Danieli, E. Otero, C. Sciancalepore, A. M. Talarico, M. A. Arrio, A. Cornia, D. Gatteschi, and R. Sessoli, Nat. Mater. **8**, 194 (2009).
[4] S. Carretta, E. Liviotti, N. Magnani, P. Santini, and G. Amoretti, Phys. Rev. Lett. **92**, 207205 (2004).
[5] P. Santini, S. Carretta, E. Liviotti, G. Amoretti, P. Carretta, M. Filibian, A. Lascialfari, and E. Micotti, Phys. Rev. Lett. **94**, 077203 (2005).
[6] S. Carretta, P. Santini, G. Amoretti, M. Affronte, A. Candini, A. Ghirri, I. S. Tidmarsh, R. H. Laye, R. Shaw, and E. J. L. McInnes, Phys. Rev. Lett. **97**, 207201 (2006).
[7] M. N. Leuenberger and D. Loss, Nature (London) **410**, 789 (2001).
[8] F. Troiani, A. Ghirri, M. Affronte, S. Carretta, P. Santini, G. Amoretti, S. Piligkos, G. Timco, and R. E. P. Winpenny, Phys. Rev. Lett. **94**, 207208 (2005).
[9] G. A. Timco, S. Carretta, F. Troiani, F. Tuna, R. J. Pritchard, C. A. Muryn, E. J. L. McInnes, A. Ghirri, A. Candini, P. Santini, G. Amoretti, M. Affronte, and R. E. P. Winpenny, Nat. Nanotechnol. **4**, 173 (2009).
[10] M. Evangelisti and E. K. Brechin, Dalton Trans. **39**, 4672 (2010).
[11] E. Garlatti, S. Carretta, J. Schnack, G. Amoretti, and P. Santini, Appl. Phys. Lett. **103**, 202410 (2013).
[12] J. W. Sharples, D. Collison, E. J. L. McInnes, J. Schnack, E. Palacios, and M. Evangelisti, Nat. Commun. **5**, 5321 (2014).
[13] J. Schnack and M. Luban, Phys. Rev. B **63**, 014418 (2000).
[14] O. Waldmann, Phys. Rev. B **65**, 024424 (2001).
[15] F. Meier and D. Loss, Phys. Rev. B **64**, 224411 (2001).
[16] J. van Slageren, R. Sessoli, D. Gatteschi, A. A. Smith, M. Helliwell, R. E. P. Winpenny, A. Cornia, A. L. Barra, A. G. M. Jansen, E. Rentschler, and G. A. Timco, Chem. Eur. J. **8**, 277 (2002).
[17] S. Carretta, J. van Slageren, T. Guidi, E. Liviotti, C. Mondelli, D. Rovai, A. Cornia, A. L. Dearden, F. Carsughi, M. Affronte, C. D. Frost, R. E. P. Winpenny, D. Gatteschi, G. Amoretti, and R. Caciuffo, Phys. Rev. B **67**, 094405 (2003).
[18] K. Bärwinkel, P. Hage, H.-J. Schmidt, and J. Schnack, Phys. Rev. B **68**, 054422 (2003).
[19] O. Cador, D. Gatteschi, R. Sessoli, F. K. Larsen, J. Overgaard, A.-L. L. Barra, S. J. Teat, G. A. Timco, and R. E. P. Winpenny, Angew. Chem., Int. Ed. **43**, 5196 (2004).
[20] S. Carretta, P. Santini, G. Amoretti, M. Affronte, A. Ghirri, I. Sheikin, S. Piligkos, G. Timco, and R. E. P. Winpenny, Phys. Rev. B **72**, 060403(R) (2005).
[21] O. Waldmann, C. Dobe, H. U. Güdel, and H. Mutka, Phys. Rev. B **74**, 054429 (2006).
[22] M. L. Baker, T. Guidi, S. Carretta, J. Ollivier, H. Mutka, H. U. Güdel, G. A. Timco, E. J. L. McInnes, G. Amoretti, R. E. P. Winpenny, and P. Santini, Nat. Phys. **8**, 906 (2012).
[23] A. Furrer and O. Waldmann, Rev. Mod. Phys. **85**, 367 (2013).
[24] G. Kamieniarz, W. Florek, and M. Antkowiak, Phys. Rev. B **92**, 140411(R) (2015).
[25] R. J. Woolfson, G. A. Timco, A. Chiesa, I. J. Vitorica-Yrezabal, F. Tuna, T. Guidi, E. Pavarini, P. Santini, S. Carretta, and R. E. P. Winpenny, Angew. Chem., Int. Ed. **128**, 9002 (2016).
[26] S. Carretta, P. Santini, G. Amoretti, T. Guidi, J. R. D. Copley, Y. Qiu, R. Caciuffo, G. Timco, and R. E. P. Winpenny, Phys. Rev. Lett. **98**, 167401 (2007).
[27] C. J. Wedge, G. A. Timco, E. T. Spielberg, R. E. George, F. Tuna, S. Rigby, E. J. L. McInnes, R. E. P. Winpenny, S. J. Blundell, and A. Ardavan, Phys. Rev. Lett. **108**, 107204 (2012).
[28] M. Affronte, A. Ghirri, S. Carretta, G. Amoretti, S. Piligkos, G. A. Timco, and R. E. P. Winpenny, Appl. Phys. Lett. **84**, 3468 (2004).
[29] G. A. Timco, E. J. L. McInnes, and R. E. P. Winpenny, Chem. Soc. Rev. **42**, 1796 (2013).
[30] R. H. Laye, F. K. Larsen, J. Overgaard, C. A. Muryn, E. J. L. McInnes, E. Rentschler, V. Sanchez, S. J. Teat, H. U. Güdel, O. Waldmann, G. A. Timco, and R. E. P. Winpenny, Chem. Commun. **2005**, 1125 (2005).
[31] G. A. Timco, E. J. L. McInnes, R. G. Pritchard, F. Tuna, and R. E. P. Winpenny, Angew. Chem., Int. Ed. **47**, 9681 (2008).
[32] J. Ferrando-Soria, E. Moreno Pineda, A. Chiesa, A. Fernandez, S. A. Magee, S. Carretta, P. Santini, I. J. Vitorica-Yrezabal, F. Tuna, G. A. Timco, E. J. L. McInnes, and R. E. P. Winpenny, Nat. Commun. **7**, 11377 (2016).
[33] T. B. Faust *et al.*, Chem. Eur. J. **17**, 14020 (2011).
[34] A. Chiesa, G. F. S. Whitehead, S. Carretta, L. Carthy, G. A. Timco, S. J. Teat, G. Amoretti, E. Pavarini, R. E. P. Winpenny, and P. Santini, Sci. Rep. **4**, 7423 (2014).
[35] G. F. S. Whitehead, F. Moro, G. A. Timco, W. Wernsdorfer, S. J. Teat, and R. E. P. Winpenny, Angew. Chem., Int. Ed. **52**, 9932 (2013).
[36] V. Corradini, A. Ghirri, E. Garlatti, R. Biagi, V. De Renzi, U. del Pennino, V. Bellini, S. Carretta, P. Santini, G. Timco, R. Winpenny, and M. Affronte, Adv. Funct. Mater. **22**, 3706 (2012).
[37] E. Garlatti, M. A. Albring, M. L. Baker, R. J. Docherty, H. Mutka, T. Guidi, V. Garcia Sakai, G. F. S. Whitehead, R. G. Pritchard, G. A. Timco, F. Tuna, G. Amoretti, S. Carretta, P. Santini, G. Lorusso, M. Affronte, E. J. L. McInnes, D. Collison, and R. E. P. Winpenny, J. Am. Chem. Soc. **136**, 9763 (2014).
[38] R. Caciuffo, T. Guidi, G. Amoretti, S. Carretta, E. Liviotti, P. Santini, C. Mondelli, G. Timco, C. A. Muryn, and R. E. P. Winpenny, Phys. Rev. B **71**, 174407 (2005).
[39] A. Ardavan, O. Rival, J. J. L. Morton, S. J. Blundell, A. M. Tyryshkin, G. A. Timco, and R. E. P. Winpenny, Phys. Rev. Lett. **98**, 057201 (2007).
[40] I. Siloi and F. Troiani, Phys. Rev. B **86**, 224404 (2012).
[41] C. Loose, E. Ruiz, B. Kersting, and J. Kortus, Chem. Phys. Lett. **452**, 38 (2008); J. Cirera, E. Ruiz, S. Alvarez, F. Neese, and J. Kortus, Chem. Eur. J. **15**, 4078 (2009).

[42] J. F. Nossa, M. F. Islam, C. M. Canali, and M. R. Pederson, Phys. Rev. B **85**, 085427 (2012); M. Islam, J. F. Nossa, C. M. Canali, and M. Pederson, *ibid.* **82**, 155446 (2010).

[43] D. W. Boukhvalov, A. I. Lichtenstein, V. V. Dobrovitski, M. I. Katsnelson, B. N. Harmon, V. V. Mazurenko, and V. I. Anisimov, Phys. Rev. B **65**, 184435 (2002); V. V. Mazurenko, Y. O. Kvashnin, F. Jin, H. A. De Raedt, A. I. Lichtenstein, and M. I. Katsnelson, *ibid.* **89**, 214422 (2014); T. Steenbock, J. Tasche, A. I. Lichtenstein, and C. Herrmann, J. Chem. Theory Comput. **11**, 5651 (2015).

[44] M. Atanasov, J. M. Zadrozny, J. R. Long, and F. Neese, Chem. Sci. **4**, 139 (2013).

[45] A. V. Postnikov, S. G. Chiuzbaian, M. Neumann, and S. Blügel, J. Phys. Chem. Solids **65**, 813 (2004); A. V. Postnikov, M. Brüger, and J. Schnack, Phase Trans. **78**, 47 (2005); A. V. Postnikov, J. Kortus, and M. R. Pederson, Phys. Status Solidi B **243**, 2533 (2006).

[46] J. Cano, R. Costa, S. Alvarez, and E. Ruiz, J. Chem. Theory Comput. **3**, 782 (2007); E. Cremades, J. Cano, E. Ruiz, G. Rajamaran, C. J. Milios, and E. K. Brechin, Inorg. Chem. **48**, 8012 (2009).

[47] V. Bellini, G. Lorusso, A. Candini, W. Wernsdorfer, T. B. Faust, G. A. Timco, R. E. P. Winpenny, and M. Affronte, Phys. Rev. Lett. **106**, 227205 (2011).

[48] D. W. Boukhvalov, V. V. Dobrovitski, M. I. Katsnelson, A. I. Lichtenstein, B. N. Harmon, and P. Kögerler, Phys. Rev. B **70**, 054417 (2004); D. M. Tomecka, V. Bellini, F. Troiani, F. Manghi, G. Kamieniarz, and M. Affronte, *ibid.* **77**, 224401 (2008).

[49] V. Bellini and M. Affronte, J. Phys. Chem. B **114**, 14797 (2010).

[50] T. Guptan and G. Rajaraman, Chem. Commun. **52**, 8972 (2016).

[51] A. Chiesa, S. Carretta, P. Santini, G. Amoretti, and E. Pavarini, Phys. Rev. Lett. **110**, 157204 (2013).

[52] Y. O. Kvashnin, O. Granas, I. Di Marco, M. I. Katsnelson, A. I. Lichtenstein, and O. Eriksson, Phys. Rev. B **91**, 125133 (2015).

[53] K. Boguslawski, K. H. Marti, Ö. Legeza, and M. Reiher, J. Chem. Theory Comput. **8**, 1970 (2012).

[54] M. Valiev, E. J. Bylaska, N. Govind, K. Kowalski, T. P. Straatsma, H. J. J. van Dam, D. Wang, J. Nieplocha, E. Apra, T. L. Windus, and W. A. de Jong, Comput. Phys. Commun. **181**, 1477 (2010).

[55] In order to reduce the computational effort we replace CH_3 groups by hydrogens, a commonly adopted procedure (see, e.g., Ref. [56]). We have previously checked in similar compounds that this approximation leads only to a slight modification of all the exchange constants, while fully preserving the hierarchy of the interactions. Furthermore, to speed up convergence (by exploiting accelerators) in odd-electron rings, such as Cr_7Ni and Cr_7Zn, it proves convenient to perform LDA calculations on a pair of distant rings, sufficiently far apart so that their interaction is negligible.

[56] V. Bellini, A. Olivieri, and F. Manghi, Phys. Rev. B **73**, 184431 (2006).

[57] S. F. Boys, Rev. Mod. Phys. **32**, 296 (1960); Boys localization minimizes the spatial extent of the orbitals by maximizing the function $\sum_{i>j} |\langle\psi_i|\mathbf{r}|\psi_i\rangle - \langle\psi_j|\mathbf{r}|\psi_j\rangle|^2$, expressed in terms of the Kohn-Sham orbitals ψ_i.

[58] For a pedagogical derivation see E. Pavarini, The LDA+DMFT Approach, in *The LDA+DMFT Approach to Strongly Correlated Materials*, edited by E. Pavarini, E. Koch, A. Lichtenstein, and D. Vollhardt (Verlag des Forschungszentrum Jülich, 2011).

[59] O. Gunnarsson, O. K. Andersen, O. Jepsen, and J. Zaanen, Phys. Rev. B **39**, 1708 (1989).

[60] For Ni^{2+} we used the typical values reported in Ref. [61] for a Ni^{2+} ion in an octahedral cage. For Cr^{3+}, we employ the value we obtained self-consistently for green Cr_8 rings [51]. For Mn^{2+}, since we could not find in the literature a screened value, we renormalized the free-ion value [61] with the same screening factor calculated for Cr^{3+} ($\sim 1/2$). All these parameters are reported in Table I.

[61] A. Abragam and B. Bleaney, *Electron Paramagnetic Resonance of Transition Metal Ions* (Clarendon, Oxford, 1970).

[62] A. H. MacDonald, S. M. Girvin, and D. Yoshioka, Phys. Rev. B **37**, 9753 (1988).

[63] M. L. Baker, G. A. Timco, S. Piligkos, J. S. Mathieson, H. Mutka, F. Tuna, P. Kozlowski, M. Antkowiak, T. Guidi, T. Gupta, H. Rath, R. J. Woolfson, G. Kamieniarz, R. G. Pritchard, H. Weihe, L. Cronin, G. Rajaraman, D. Collison, E. J. L. McInnes, and R. E. P. Winpenny, Proc. Natl. Acad. Sci. U.S.A. **109**, 19113 (2012).

[64] C. M. Casadei, L. Bordonali, Y. Furukawa, F. Borsa, E. Garlatti, A. Lascialfari, S. Carretta, S. Sanna, G. Timco, and R. Winpenny, J. Phys.: Condens. Matter **24**, 406002 (2012).

[65] E. Micotti, Y. Furukawa, K. Kumagai, S. Carretta, A. Lascialfari, F. Borsa, G. A. Timco, and R. E. P. Winpenny, Phys. Rev. Lett. **97**, 267204 (2006).

[66] T. Guidi, B. Gillon, S. A. Mason, E. Garlatti, S. Carretta, P. Santini, A. Stunault, R. Caciuffo, J. van Slageren, B. Klemke, A. Cousson, G. A. Timco, and R. E. P. Winpenny, Nat. Commun. **6**, 7061 (2015).

[67] F. Troiani, S. Carretta, and P. Santini, Phys. Rev. B **88**, 195421 (2013).